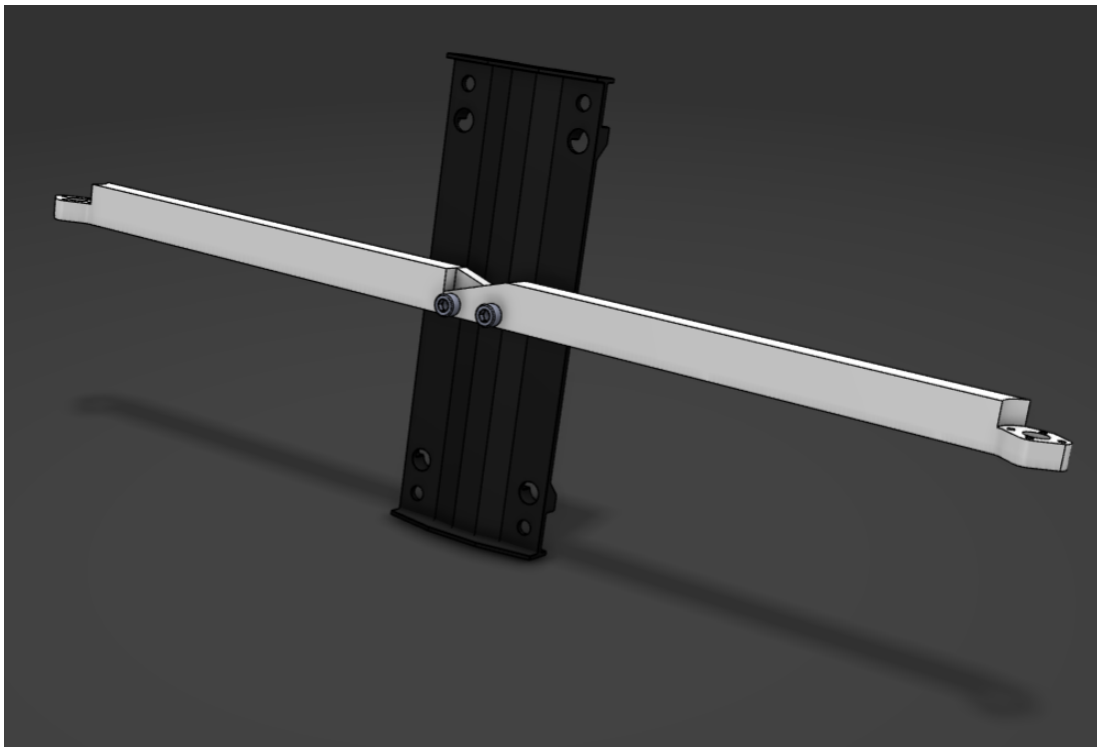


# Engineering Practice 2 DBT Design Report

Group 08



26/05/2021

# Contents

List of Figures .....	2
List of Tables.....	3
List of Symbols .....	4
1. Introduction .....	5
2. Design/Multidisciplinary Optimisation Approach .....	5
3. Structural Concept Design .....	5
3.1. Problem Definition.....	5
3.2. Objectives.....	5
3.3. Variables .....	6
3.4. Analysis Using Beam Theory .....	6
3.5. Cross-Sectional Shape of Arm .....	6
3.6. Arm–Mounting-Plate Interface .....	7
3.7. Electric Motor Mount.....	7
3.8. Optimising Print Settings .....	7
3.9. Finite Elements Validation and Optimisation .....	8
3.10. Final Results and Predicted Performance .....	8
4. Control Law .....	9
4.1. Preliminary Simulink Model Design .....	9
4.2. Physics Model Development.....	9
4.3. Controller Selection and Tuning .....	10
.....	11
4.4. Final Results and Predicted Performance .....	11
References .....	12
Appendix A – Mesh Convergence Study.....	13
Appendix B – Final Mass Breakdowns.....	14
Appendix C – Predicted Controller Performance with Different System Delays.....	15

## List of Figures

Figure 1. Von Mises Stress Distribution, showing maximum stresses in the region.....	8
Figure 3. Final FEA result, showing displacement over the beam. ....	8
Figure 2. Final FEA result, showing Von Mises Stress over the beam. ....	8
Figure 4. Theoretical Simulink model. ....	11
Figure 5. Predicted duo-copter response to sample mission profile with a system delay of 1 s..	11
Figure 6. FEA mesh convergence analysis for final arm design.....	13
Figure 7. Predicted duo-copter response to sample mission profile with a system delay of 0.5 s. .....	15
Figure 8. Predicted duo-copter response to sample mission profile with a system delay of 1.5 s. .....	15

## List of Tables

Table 1. Comparison of the shape factors.....	6
Table 2. Final print settings.....	7
Table 3. Mass breakdown per arm. ....	14
Table 4. Mass breakdown for the constant mass of the duo-copter cart. ....	14

## List of Symbols

$E$	Flexural modulus
$I$	Second moment of inertia
$F$	Force exerted by motors
$\delta$	Tip deflection
$L$	Length of arm
$A$	Cross-sectional area
$M$	Bending moment
$\phi_B^e$	Shape factor in elastic bending
$\sigma_{max}$	Flexural strength of print material
$\sigma^*$	Flexural strength of cellular solid
$\rho^*/\rho$	Infill density
$d$	Diameter of bolt hole
$D$	Height of mounting plate interface
$t$	Thickness of mounting plate interface
$m$	Mass
$h$	Height of duo-copter
$\mu$	Coefficient of dynamic friction
$N$	Normal force acting on pads of cart
$T$	Thrust produced by motor-prop assemblies
$W$	Weight of duo-copter payload
$x$	Distance between centre of gravity of structural member and mounting plate
$L$	Height of mounting plate

## 1. Introduction

This report outlines the thought processes behind the design and optimisation of a structural member for a duo-copter constrained to vertical motion and a control law which tracks altitude commands. The aim of the designs is to allow the structural member of the duo-copter to connect the payload to its propulsive system and for the duo-copter to follow an unknown mission profile. The key objectives of the structural design and the control law of the duo-copter are to:

- minimise manufacturing costs
- maximise the accuracy in which the mission profile is followed
- minimise energy consumption when completing the mission profile.

Each of these three main objectives are optimised differently, and therefore a focus was placed on finding necessary compromises which results in a balanced final design of the structural member and the control law.

## 2. Design/Multidisciplinary Optimisation Approach

The team was divided into a structures sub-team and a control sub-team. The two sub-teams each held daily meetings to progress their respective sections of the project and regular meetings between the sub-teams were also held to discuss, critique, and evaluate the designs as a whole.

The structures sub-team were responsible for developing designs for the structural member with the objective of minimising cost, including different ways in which the structural member can be attached to the mounting plate of the cart containing the duo-copter. The sub-team approached the problem by defining objectives for the final structural design to meet, before doing basic structural calculations to give approximate dimensions for the structural member. The structures sub-team then modelled the structural member in Dassault Systèmes 3DEXperience and carried out finite element analysis (FEA) to visualise its internal stresses and displacement based on the forces (thrust from the motor-prop assemblies and weight of the duo-copter payload) it will likely experience. This data was then used to minimise the mass of the structure, whilst keeping within the already-defined structural design objectives. The stiffness-oriented structural design objective had to be met to ensure the thrust produced by the motors were as close to that modelled in Simulink by the control sub-team as possible.

The control sub-team approached the control law design by firstly creating a preliminary Simulink model, before developing the physics model of the duo-copter and the testing apparatus. A focus was placed on modelling the varying mass of the cable tracks, the friction forces and the time delays within the system. Other factors such as slack within the rope connecting the carts and aerodynamic effects from the propellers were also considered. The theoretical Simulink model, which includes a Smith predictor with a PID controller and a plant, was then developed further based on the physics model to simulate the real-life dynamic response of the duo-copter in the actual testing apparatus as accurately as possible. This Simulink model then allowed the tuning of the PID controller to be completed. The energy consumption and tracking accuracy of the duo-copter were analysed during the tuning process, along with the actual and desired height of the duo-copter associated with a sample mission profile, which allowed the duo-copter's performance to be predicted for each set of PID gains. The best set of gains, based on the tracking accuracy and energy consumption objectives, and how well they account for uncertainties within the system were then selected.

## 3. Structural Concept Design

### 3.1. Problem Definition

The arm of the duo-copter is an essential structural member upon which the electric motors are mounted. It is required that the motors be at least 0.50 m apart, which means that due to print volume limitations, two 0.25 m arms will be printed separately. Each arm can initially be simplified as a cantilever beam with a force applied at one end and constrained by a fixed support at the other.

### 3.2. Objectives

The design should:

1. Be able to withstand forces and moments due to the typical loading conditions of the duo-copter. The typical loading conditions are: 1) payload weight; 2) propulsive forces exerted by the electric motors; 3) impact force if the duo-copter falls from the maximum height of the testing apparatus.

2. Be as stiff as possible to minimise tip deflection to ensure that >95% of thrust from the electric motors act in the vertical direction.
3. Minimise manufacturing costs when additively manufactured using material extrusion. This implies that the final structure should be as light as possible (least material used) while also minimising the amount of support material needed during 3D printing.

### 3.3. Variables

The design parameters to be varied are as follows:

1. Cross-sectional shape of the arm. Since the print material is fixed, the flexural stiffness of the arm will be determined by its cross-sectional shape. Shapes with higher second moments of inertia result in a stiffer arm, reducing tip deflection. While certain shapes may decrease the weight of the arm, overall mass and cost will increase if too much support material is required for printing.
2. Print density. Printing parameters such as infill density, infill pattern and number of wall layers affect the density of the component. Higher print density will increase manufacturing costs and print time while lower print density may reduce structural performance.

### 3.4. Analysis Using Beam Theory

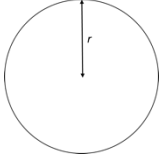


Beam Theory was used to analyse each duo-copter arm, which is modelled by a 0.25 m long beam of constant flexural stiffness  $EI$ , constrained at one end ( $z = 0$  m) by a fixed support, and with an upwards force  $F = 10.80$  N (maximum upwards thrust) applied at the other end ( $z = L = 0.25$  m).

The bending moment,  $M$  /Nm along the length of the arm follows the equation:  $M = -F(L - z)$  and the tip deflection,  $\delta$  /mm follows the equation:  $\delta = \frac{FL^3}{3EI}$ . For >95% vertical thrust, the maximum deflection under maximum thrust output is 13.16 mm. This corresponds to a minimum second moment of area,  $I = 3.054 \times 10^{-9} \text{ m}^4$ , since the flexural modulus of the print material is  $E = 1.4$  GPa.

### 3.5. Cross-Sectional Shape of Arm

Due to the anisotropy introduced by infills, FEA of complex geometries may not be an accurate representation of the performance of the final product and so it was decided that this should be avoided. In addition, cost restrictions limit the effectiveness of truss structures, as they require large amounts of support when printed in their final orientation, increasing cost without providing any structural gain in the final product. This was verified using 3DEXPERIENCE's Functional Generative Design Product, which, for a similar tip deflection, had lower final mass but cost more to manufacture due to the amount of support material required. It was thus decided to design an arm with constant cross-sectional shape.

Table 1. Comparison of the shape factors.

Cross-Sectional Shape	Circle	Rectangle	Triangle
			
Second Moment of Area, $I$	$\frac{\pi r^4}{4}$	$\frac{bh^3}{12}$	$\frac{bh^3}{36}$
Shape Factor, $\varphi_B^e$	1	$\frac{\pi h}{3b}$	$\frac{2\pi h}{9b}$
Rank	3	1	2

To guide the selection of the cross-sectional shape, three basic shapes were considered and their shape factor for elastic bending,  $\varphi_B^e$ , was compared as seen in Table 1. A higher shape factor means less material can be used for a given stiffness or strength [1].  $\varphi_B^e$  is calculated by taking the ratio of bending stiffness to

that of a reference circular section with the same cross-sectional area, which reduces to  $\varphi_B^e = \frac{4\pi I}{A^2}$ . For the same ratio of width to height as the triangle, the rectangular cross-section had the highest shape factor and was thus chosen to be the cross-sectional shape of the final arm design.

### 3.6. Arm–Mounting-Plate Interface

The dimensions of the arm–mounting-plate interface were determined to withstand stress due to in-plane bending at the edge of the holes in which the M6 mounting screws will be inserted. It was decided that each arm would accept both bolts, in order to reduce the stresses around each hole in the plastic and to allow for potential failure of one hole, without the entire arm failing.

The holes were sized to withstand stress up to the flexural strength of the print material ( $\sigma_{max} = 50$  MPa), using equation (1), as seen in [2]:

$$\sigma_{max} = \frac{12Md}{(D^3 - d^3)t} \quad (1)$$

where  $M = 2.7$  Nm is the bending moment at  $z = 0$  m,  $d = 6$  mm is the diameter of the hole for the M6 screw, and  $D$  and  $t$  are the height and thickness of the interface respectively. It was found that  $D = 10$  mm and  $t = 5$  mm satisfy the equation above. In order to account for the infill density of the arm, the thickness was scaled using equation (2) [3].

$$\sigma^* = 5.2 * \left( \frac{2}{\sqrt{3}} \frac{\rho^*}{\rho} \right)^3 * E \quad (2)$$

where  $\sigma^*$  denotes the strength of the cellular solid,  $\frac{\rho^*}{\rho}$  is the infill density, and  $E$  is the Flexural Modulus of the solid material. Comparing  $\sigma_{max}$  and  $\sigma^*$  gave a scaling factor of 1.34, which was increased to 1.5 in case of imperfections in the 3D printing process. Adjustment of the height and thickness of the mount to account for the scaling factor gave a final height of  $D = 10$ mm and thickness of  $t = 7.5$ mm.

### 3.7. Electric Motor Mount

To reduce the size of the motor mount, the mount was designed using FEA results. The motor mount was gradually reduced in thickness until the stresses approached the yield stress of the cellular solid as calculated using equation (2).

### 3.8. Optimising Print Settings

Aside from the size and geometry of the printed component, print settings also affect the weight of the component as well as the print time. It was found that printing a solid fill significantly increases the weight of the arm, cost of manufacture and print time without benefiting the structural performance since stresses along the arm are not constant. As such, the hexagonal fill was chosen, forming an out-of-plane honeycomb sandwich structure, commonly used in aerospace applications [4]. This led to a significant reduction in weight, without compromising stiffness [5]. The hexagonal infill provided the best strength-to-weight ratio of all the available infills and allowed for the lowest infill density (18%). To improve the stiffness of the component, the thickness of the roof and floor layers were increased, and the wall thickness reduced. This is analogous to increasing the flange thickness of an I-beam, which increases the distribution of mass away from the centroid, thus improving stiffness [6]. The final print settings are detailed in Table 2. To account for shrinkage of the material during 3D printing, the diameters of the bolt holes on the mounts were increased by 0.1mm [7] in the design submitted for printing.

Table 2. Final print settings.

Layer Height/mm	Infill Pattern	Infill Density/%	Roof and Floor Layer Thickness/mm	Wall Layer Thickness/mm
0.1	Hexagons	18	1.0	0.4



### 3.9. Finite Elements Validation and Optimisation

For the FE validation, the arm was modelled as a shell, with only the walls and the roof and floor of the correct thickness. This was done as the honeycomb infill has less impact on the bending response of the beam compared to the shell [8]. Furthermore, the infill was generated in the slicer software, making the exact pattern hard to replicate, which could cause overestimation of the beam's performance. Initially, the basic cantilever beam was modelled and an FEA analysis was performed, with a base size of 0.9 mm. This showed very good agreement with the theoretical values, and so further development was undertaken. The beam section and mounting section were then combined, and tested in a more representative manner of the actual loading, with the restraints being modelled as M6 bolts attached to the ground, and the motor thrust as acting from the centre line of the arm, 250 mm from the middle of the two mounting holes, as it would be in the final design. This highlighted high deformation and stress concentrations at the sharp corner between the two sections, which was resolved by chamfering the corner to reduce the stresses as seen in Figure 1. This reduced the deformation at the tip by half, within our constraint of  $\delta = 13.16$  mm, and the maximum stress by 4.5 times the previous value, reducing the chance of delamination in the layers in the 3D print around the bolt holes.

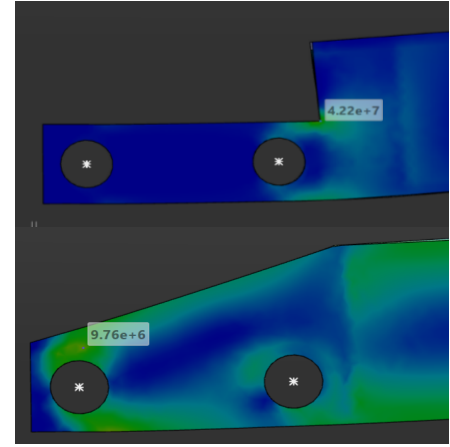


Figure 1. Von Mises Stress Distribution, showing maximum stresses in the region.

The motor mount region was then modified to be 10 mm high, at a radius of 14.1 mm from the centre of the motor, allowing it to sit on the mount and to allow the maximum amount of thread engagement with the motor and the 18 mm M3 screws. As this was close to the final design, a more sophisticated model was adopted for the FEA. The motor mass was modelled as a point load acting vertically downward at the centre point of the mounting region, and the thrust force was modelled as a distributed force acting over the area of the M3 screw heads vertically, amounting to a total force of 6.935 N, the largest thrust force the controller produces. The mass of the ESC was modelled as acting vertically downward at a distance of 150 mm from the motor towards the mounting plate side of the arm, which was the distance of the wires estimated from the video provided, and the self-weight of the arm was modelled using 3DEX's inbuilt function. Finally, the faces of the arm which would be coincident with either the other arm or the face of the motor mount were constrained. The final analysis of the arm gives a max deflection of 6.38 mm and a maximum stress of 8.73 MPa as seen in Figures 2 and 3. A mesh convergence study was then carried out, the results of which can be found in Appendix A, which verifies the validity of the FEA.

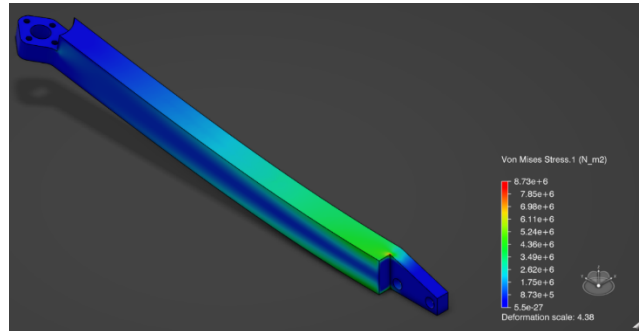


Figure 3. Final FEA result, showing Von Mises Stress over the beam.

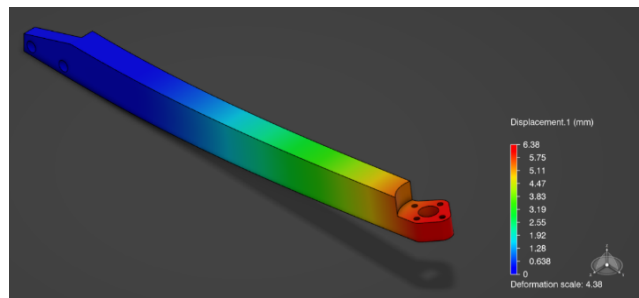


Figure 2. Final FEA result, showing displacement over the beam.

### 3.10. Final Results and Predicted Performance

As can be seen from Figure 2, the final FEA analysis predicted a maximum displacement of 6.38 mm, which gives 97.6% of thrust produced by the motor-prop assemblies to act directly upwards. As the FEA simulation can be seen to have converged from the mesh analysis, it is likely that the manufactured beam will behave in a similar manner. Figure 3 shows the Von Mises Stress distribution over the final beam design. The maximum stress can be seen to be 8.73 MPa, which is well under the flexural strength of Nylon

White of 50 MPa. In the manufactured arm there are likely to be pores and discontinuities in the plastic which will reduce the Young's Modulus and Yield Strength compared to the simulated material. However, the FEA shows that the stresses are well under yield and so the imperfections are very unlikely to cause the arm to fail under the applied loading. The infill used is also likely to result in a slightly higher value of  $I$  than in the FEA, which will further reduce the deflection of the arm.

## 4. Control Law

### 4.1. Preliminary Simulink Model Design

A preliminary Simulink model was set up using a Smith predictor with a PID controller and a plant to simulate the real-life dynamic response of the duo-copter. The Smith predictor was implemented to track altitude commands by generating a throttle control output (ranging from 0-100), based on the error between the altitude setpoint (the desired height) and the actual height. The plant takes the throttle command as input, obtains acceleration by applying balance of forces vertically and integrates it twice to obtain the actual height. Two reset logics were used within the duo-copter plant to set the boundary conditions of the duo-copter: one to reset acceleration if the acceleration is larger than zero when duo-copter is at 1.44 m or if the acceleration is smaller than zero when duo-copter is at 0 m; the other is to reset velocity when the duo-copter cart reaches the upper and lower boundaries of the track. The physics model was then developed which best simulates the properties of the duo-copter cart and the testing apparatus and implemented into this model. As 97.6% of the thrust produced by the motor-prop assemblies act in the vertical direction (mentioned in section 3.10.), this decrease in thrust from the deflection of the structural member was treated as negligible.

### 4.2. Physics Model Development

The physics model was developed by firstly considering the constant masses of the components which make up the duo-copter, which was summed to be 740.48 g (refer to Appendix B for mass breakdown). This mass includes the effective mass of the cart, the structural member, all the required screws, the ESCs and the motor-prop assemblies. The varying mass of the two cable tracks used to deliver power to the motors held by the cart containing the duo-copter was then considered, and was modelled to vary linearly with the height of the cart. The mass of one of the cable tracks being held by the cart was approximated to be:

$$m_{\text{cable held by cart}} = 0.4983 \cdot m_{\text{cable}} \cdot h + 0.2824 \cdot m_{\text{cable}} \quad (3)$$

where  $m_{\text{cable}}$  is the total mass of one of the cable tracks (190 g) and  $h$  is the altitude of the duo-copter cart. This expression was determined from estimations of the mass of one cable track held by the cart at a height of 0 m and at 1.44 m. At 0 m, the mass of one of the cable tracks held by the cart was estimated to be 53.656 g and at 1.44 m, it was assumed to be 190 g. The length of one cable track held by the cart at 0 m was estimated to be 0.2824 m of the 1 m long cable track, and so it was assumed that 28.24% of the mass of one cable track would be held by the cart at 0 m – this value came to be 53.656 g. At the maximum height of 1.44 m, it was assumed that the cart would be experiencing the full mass of the cable tracks, which is 190 g per cable track. The constant mass of the cart was then summed with the varying mass of the two cable tracks and used to calculate the total weight always acting downwards on the cart containing the duo-copter.

When modelling friction forces, a static friction up to a maximum of 130 g per cart is always present when the duo-copter's velocity is zero, and always opposes the direction of motion. Therefore, the static friction of both the cart containing the duo-copter and the counterweight cart were considered for the physics model. The dynamic friction forces were then estimated using:

$$F_{\text{dyn. friction}} = \mu N \quad (4)$$

where  $\mu$  is the coefficient of dynamic friction and  $N$  is the normal force acting on the pads at the corners of the cart. To find  $N$ , a beam theory analysis on the mounting plate of the two carts is then carried out, assuming the mounting plate behaved like a beam and the pads behaved like roller supports. For the cart containing the duo-copter, the thrust force and weight acting on the cart was considered, and moment equilibrium was taken around the top and bottom pads to give a normal force expression of:

$$N = \frac{(T - W)x}{L} \quad (5)$$

acting at the top two pads, and a normal force expression of:

$$N = -\frac{(T - W)x}{L} \quad (6)$$

acting at the bottom two pads. In equations (5) and (6),  $T$  and  $W$  are the thrust produced by the motor-prop assemblies and the total weight of the cart containing the duo-copter respectively,  $x$  is the horizontal distance between the centre of gravity of the forces acting on the structural member and the mounting plate (7.6245 mm) and  $L$  is the height of the mounting plate (210.4 mm). Equation (4) is then used to determine the dynamic friction force opposing the motion resulting from the top two pads and the bottom two pads of the mounting plate when the velocity of the duo-copter is non-zero, using the absolute values of the normal force resulting from equation 5 and 6. Absolute values were used for the normal force as the dynamic friction force always opposes the motion. The normal force acting on the pads of the counterweight cart was assumed to be negligible due to the extremely small distance between the pads and where the forces act on the counterweight cart.

The possibility of slack appearing within the tether connecting the two carts during a fast ascend of the duo-copter was then considered. The appearance of slack may result in unpredictable behaviour within the system and therefore it was decided that it would be beneficial to prevent this slack from forming. As slack would only form when the upward acceleration of the cart with the duo-copter is greater than the downward acceleration of the counterweight cart (which is equal to  $9.81 \text{ m/s}^2$ ), a constraint was placed on the maximum upward acceleration of the duo-copter, which equates to an upper throttle limit of roughly 80 in the Simulink model. Limiting the throttle to 80 would also assist with decreasing overall energy consumption as the power required to by the motors are the largest at the highest throttle commands (80 to 100), as given in Figure 2 of the DBT handout [9].

Research was also conducted to identify if aerodynamic effects from the propellers could cause significant differences between the behaviours of the simulated and real duo-copter carts. From the research, the vortex ring state phenomenon was identified as a potential cause for unpredictable behaviour resulting from the aerodynamic effects of the propellers. Vortex ring state occurs when a rotorcraft descends into its own wake fast enough to cause the vortices contained in it to be pushed inside the rotor. This causes aperiodic and strong thrust fluctuations and an abrupt loss of lift [10]. To avoid entering this dangerous state, it is necessary to limit the descent velocity of the duo-copter to half the induced velocity in the rotor (as indicated by the Drees & Hendal boundary [10]). This was done by setting a lower throttle limit of 18.

The effects of the added constraints to prevent slack and unpredictable aerodynamic effects from the propeller's disturbed air were then examined and it was found that they did not have a significant impact on the effectiveness of the simulated control system. However, these constraints should greatly reduce the uncertainties associated with slack and disturbed airflow in the real experiment and was determined to be a necessary addition to the Simulink model.

### 4.3. Controller Selection and Tuning

A PID controller designed in the Smith predictor configuration was used in our model as the large time delay of the motor has a great impact on the stability of the system. This means that if a standard PID controller was used, the control gains have to be very small, which makes the system very sensitive to error. However, with the Smith predictor, it is possible to tune the PID in a delay-free model and thus make the model more robust. The basic principle of the Smith predictor is that the desired output from a controlled system with some delay  $t$  is the same as that from the delay-free system, only with a delay of  $t$  (see [11] for more detail on the Smith predictor). The theoretical Simulink model built based upon this principle is shown in Figure 4 (where the physics model and boundary conditions were set within 'Duo-copter plant'). The control law was designed in the same way but with the delayed height from the analytical estimation changed to actual height received by the sensor.

A delay of 1.0 s was chosen as the estimated time delay (delay used for the control process), as from the provided Excel sheet with the motor data, the delay ranges from 0.5 s to 1.5 s. The tuning process was then conducted with a sample mission profile to make sure the controller gains work when the system delay (the actual delay in the system) is ranging from 0.75 s to 1.25 s. The sample mission profile was made to be complex so that if a particular set of controller gains provided a good simulated response for the sample mission profile, it would also provide an acceptable response for any other unknown mission profiles,

allowing the main aim of the control law design to be achieved. The final PID gains were determined to be  $K_p = 18$ ,  $K_i = 20$ ,  $K_d = 13$  and a filter coefficient of 70. This set of gains also provided an acceptable response when tested with an estimated time delay of 0.5 s with system delays of 0.25 s to 0.75 s, and with an estimated time delay of 1.25 s with system delays of 1.0 s to 1.5 s. These extra tests were carried out to take into account the uncertainties associated with the time delays of the system. The tests ensure that the gains would still work if the actual motor delay is out of the range of 0.75 s to 1.25 s, which would allow the correct adjustments to be made between the first and second attempts of the experiment. This set of gains were also tested on a model with small changes in mass and friction to incorporate any uncertainties resulting from the mass and/or friction estimations. The performance of the controller remained unaffected, suggesting the control law design is robust and reliable.

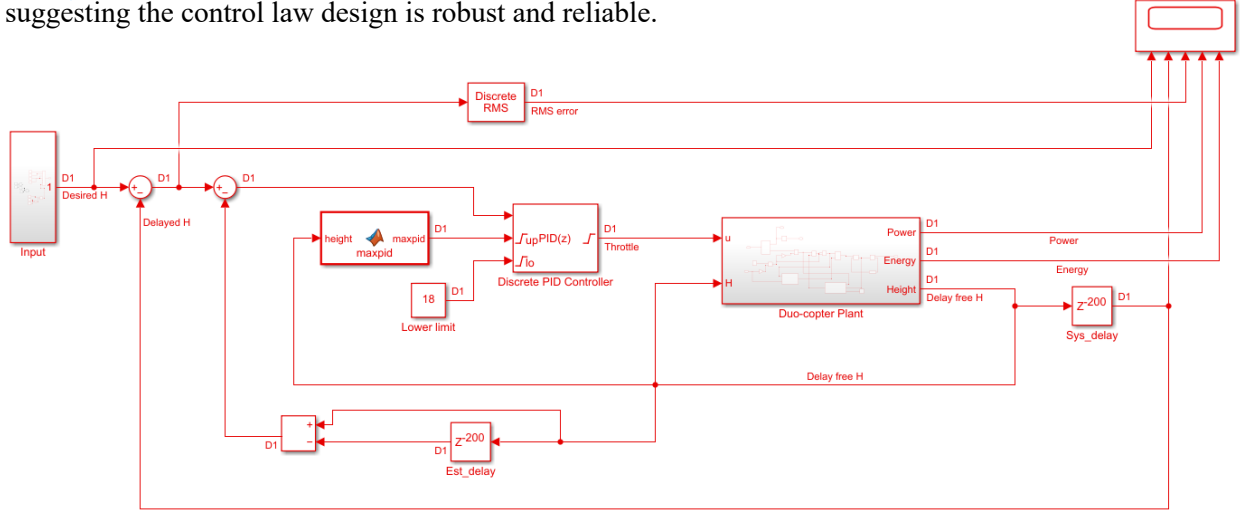


Figure 4. Theoretical Simulink model.

#### 4.4. Final Results and Predicted Performance

The energy consumption of the duo-copter was obtained by integrating the power consumption as a function of throttle inputs (Figure 2 of [9]), while the tracking accuracy of the duo-copter was monitored through obtaining the root mean square error between the simulated actual height of the duo-copter height and the desired height. The final tuning was based on maximising tracking accuracy, as it was observed

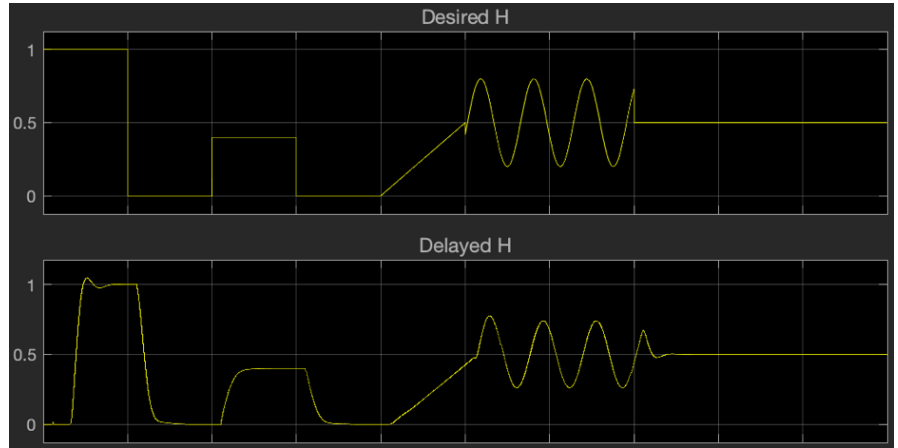


Figure 5. Predicted duo-copter response to sample mission profile with a system delay of 1 s.

that the energy consumption of the duo-copter for a certain sample mission profile maintained the same order of magnitude (around 20 kJ for the sample mission profile used for tuning). The final controller gains of  $K_p = 18$ ,  $K_i = 20$ ,  $K_d = 13$  and a filter coefficient of 70 gave the simulated duo-copter response shown in Figure 5 for a system with 1 s time delay, where the upper graph indicates the sample mission profile created for tuning, and the lower graph indicates the duo-copter's simulated response. It can be seen that the response follows the sample mission profile very closely, indicative of a high degree of tracking accuracy and therefore small root mean square error between the desired and actual height. The predicted performance of other time delays (0.5 s and 1.5 s) can be found in Appendix C. Focusing on obtaining a set of controller gains which work for a range of time delays have resulted in the most optimal control law, as it effectively accounts for the unavoidable uncertainties present in the experimental duo-copter system.

## References

- [1] M. Ashby. (2005) *Materials Selection in Mechanical Design*. 3rd Edition, Butterworth-Heinemann.
- [2] W. D. Pilkey. (2005) *Formulas for Stress, Strain, and Structural Matrices*. 2nd Edition, John Wiley & Sons.
- [3] L. Gibson & M. Ashby. (1997) The mechanics of honeycombs. In: *Cellular Solids: Structure and Properties* (Cambridge Solid State Science Series, pp. 93-174). Cambridge: Cambridge University Press. doi:10.1017/CBO9781139878326.006.
- [4] A. Krzyzak, et. al., (2016) *Sandwich Structured Composites for Aeronautics: Methods of Manufacturing Affecting Some Mechanical Properties*. International Journal of Aerospace Engineering.
- [5] P. Joyce (2003) *Sandwich Constructions Mechanical Engineering*. School of Engineering and Weapons, United States Naval Academy.
- [6] Markforged, *3D Printing Settings Affecting Part Strength*. Available from: <https://markforged.com/resources/learn/design-for-additive-manufacturing-plastics-composites/understanding-3d-printing-strength/3d-printing-settings-impacting-part-strength#:~:text=Layer%20height%20in%203D%20printing,layers%20have%20fewer%2C%20thicker%20extrusions> [Accessed 20 May 2021].
- [7] Markforged, *3D Printing Design Tips*. Available from: <https://markforged.com/resources/learn/design-for-additive-manufacturing-plastics-composites/3d-printing-strategies-for-composites/composites-3d-printing-design-tips#:~:text=Free%20Fit%20Tolerance%3A%200.10%20mm,or%20rotate%20easily%20when%20assembled> [Accessed 23 May 2021].
- [8] Rao, et. al., *Bending Behavior of Aluminum Honey Comb Sandwich Panels*. International Journal of Engineering and Advanced Technology (IJEAT), Volume-1, Issue-4, April 2012.
- [9] E. Levis. (2021) *Engineering Practice 2 – DBT Exercise*. Department of Aerospace Engineering, Imperial College London.
- [10] M. Ribera & R. Celi. (2006) Simulation Modeling in Climbing and Descending Flight with Refined Aerodynamics. In: AHS International, *62<sup>nd</sup> Annual Forum Proceedings, May 2006, Phoenix, AZ*. Department of Aerospace Engineering, University of Maryland, College Park.
- [11] C. Brown & D. J. Coombs. *Notes on Control with Delay*. Available from: <https://urresearch.rochester.edu/fileDownloadForInstitutionalItem.action?itemId=4664&itemFileId=7020> [Accessed 25 May 2021].
- [12] Industrial Tools Agency. (2019) *Weight & Count Chart Of Popular Fasteners*. Available from: <https://itafasteners.com/weight-chart.php> [Accessed 24 May 2021].

## Appendix A – Mesh Convergence Study

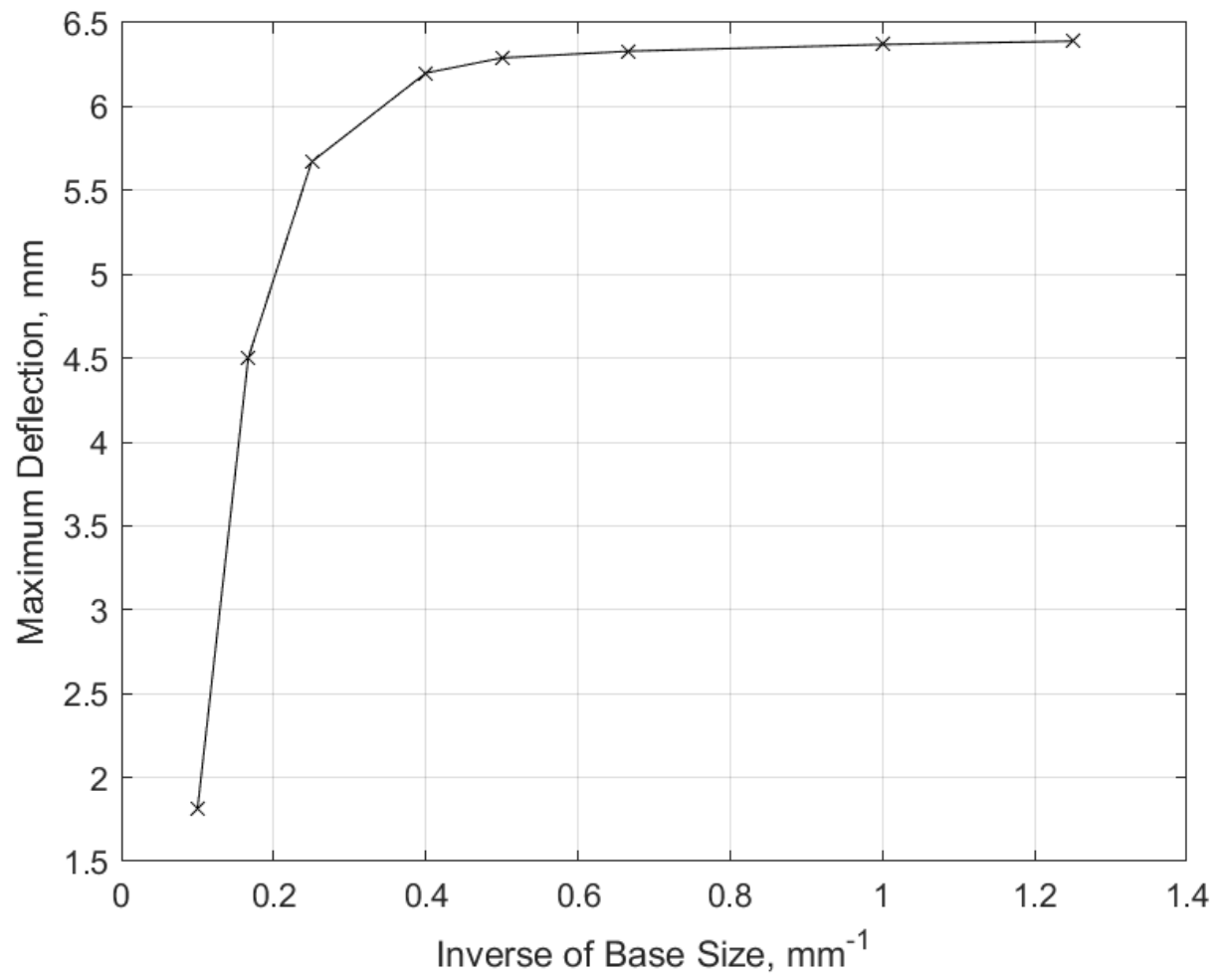


Figure 6. FEA mesh convergence analysis for final arm design.

## Appendix B – Final Mass Breakdowns

Table 3. Mass breakdown per arm.

Component	Component Mass, g	Units of Component	Total Mass, g
3D Printed Arm	21.84	1	21.84
M3 × 12mm Screws	9.60 [12]	4	38.40
ESC	51.00	1	51.00
Motor and Prop	101.00	1	101.00
		<b>Total Mass, g</b>	212.24

Table 4. Mass breakdown for the constant mass of the duo-copter cart.

Component	Component Mass, g	Units of Component	Total Mass, g
Arm	212.24	2	424.48
M6 × 30mm Bolts	83.00 [12]	2	166.00
Effective Mass of Duo-copter Cart	150.00	1	150.00
		<b>Total Mass, g</b>	740.48

## Appendix C – Predicted Controller Performance with Different System Delays

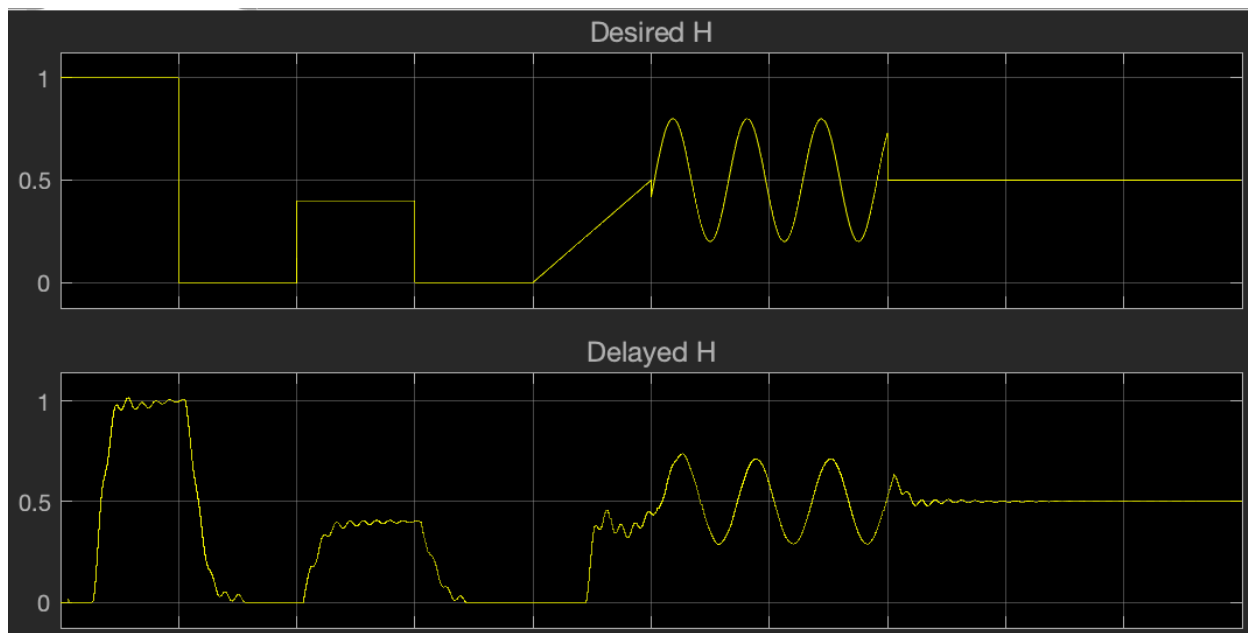


Figure 7. Predicted duo-copter response to sample mission profile with a system delay of 0.5 s.

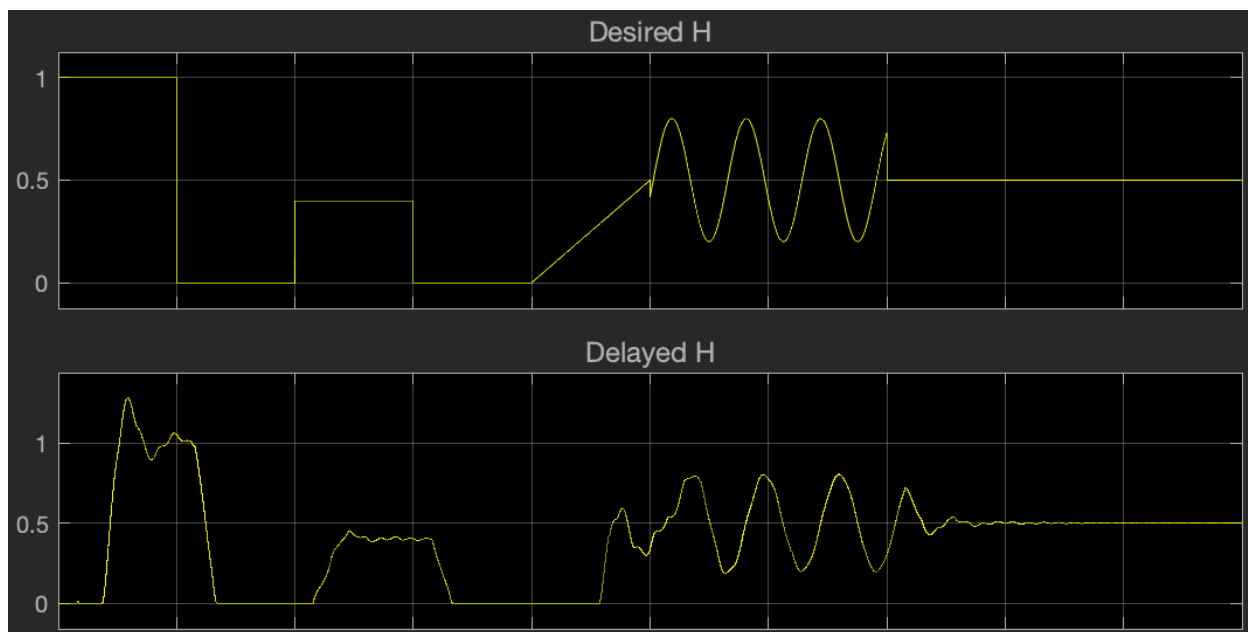


Figure 8. Predicted duo-copter response to sample mission profile with a system delay of 1.5 s.